

PAPER

Effect of seed and interlayer Pt thickness on spin-orbit torque efficiency in Co/Pt multilayer with perpendicular magnetic anisotropy

To cite this article: Gerard Joseph Lim *et al* 2020 *J. Phys. D: Appl. Phys.* **53** 505002

View the [article online](#) for updates and enhancements.



IOP | ebooks™

Bringing together innovative digital publishing with leading authors from the global scientific community.

Start exploring the collection—download the first chapter of every title for free.

Effect of seed and interlayer Pt thickness on spin-orbit torque efficiency in Co/Pt multilayer with perpendicular magnetic anisotropy

Gerard Joseph Lim , Weiliang Gan  and Wen Siang Lew

School of Physical and Mathematical Sciences, Nanyang Technological University, 21 Nanyang Link, 637371, Singapore

E-mail: wensiang@ntu.edu.sg

Received 23 April 2020, revised 14 July 2020

Accepted for publication 6 August 2020

Published 25 September 2020



CrossMark

Abstract

As-deposited [Co/Pt] multilayers show strong perpendicular magnetic anisotropy (PMA) and spin-orbit torque (SOT). However, such structures require properly textured Pt (111) seed layers and optimized interlayer Pt thicknesses in order to maximise both PMA and SOT efficiency. In this work, the interplay of seed and interlayer Pt thickness on PMA and SOT efficiency in Ta/Pt/[Co/Pt]₃/Co/Ta multilayers was studied. Using the harmonic lock-in method, the SOT damping- and field-like efficiencies were determined, with corrections for current shunting as well as the planar Hall effect. Our measurements show that the corrected effective SOT efficiencies are at least twice as large as the uncorrected values, with damping-like efficiency of up to ~ 22 Oe per 10^{10} A m⁻², which scales inversely with the Pt seed and interlayer thicknesses due to screening of the spin current originating from the high-resistivity bottom β -Ta layer. The choice of Pt seed and interlayer thicknesses is a compromise between PMA and SOT efficiency of the device.

Supplementary material for this article is available [online](#)

Keywords: spin-orbit torque, perpendicular magnetic anisotropy, multilayer

(Some figures may appear in colour only in the online journal)

1. Introduction

Current-induced spin-orbit torques (SOTs) have been demonstrated in bilayer systems of ultrathin ferromagnetic (FM) layers such as Co interfaced with a heavy-metal (HM) layer such as Pt [1]. The Pt/Co bilayer structure allows for Pt-induced (111) crystallinity and low lattice mismatch with Co, both of which are necessary to achieve as-deposited perpendicular magnetic anisotropy (PMA) with large effective magnetic anisotropy K_u [2–6]. These factors favour scalability as well as thermal stability Δ , which is given by $\Delta = K_u V / k_B T$, where V is the magnetic volume, k_B is the

Boltzmann constant, and T is the temperature. Driving a charge current through devices with such structures generates torques that lead to highly efficient magnetization switching [1, 7]. As such, manipulating magnetization using SOT has great prospects for low-power spintronic memory and logic applications [8, 9].

The SOTs that arise from such structures with inversion asymmetry stem from the spin current due to the spin Hall effect (SHE) and the effective magnetic field due to the Rashba effect. HM/FM bilayer structures have been studied in order to isolate sources of SOT and quantify SOT efficiencies [10–12]. By parameterizing the SOT efficiency in terms of the spin

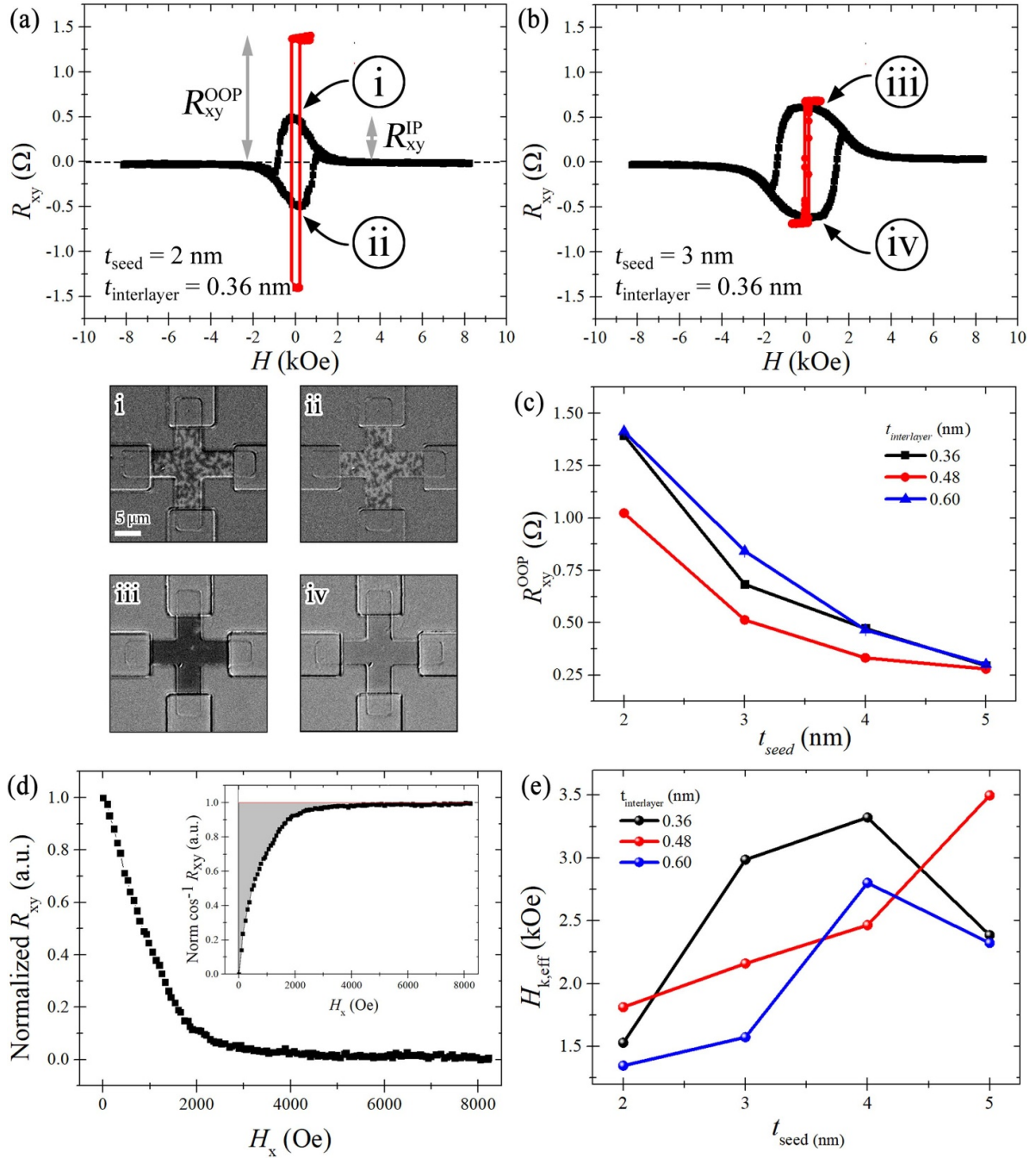


Figure 1. (a), (b) Anomalous Hall resistance R_{xy} in a sweeping in-plane field H_x (black) and out-of-plane field H_z (red) across varying t_{seed} and $t_{interlayer}$. All devices show PMA with square hysteresis loops in H_z . Kerr images (i)—(iv) show the respective remanent z -magnetization state at $H_x = 0$ Oe. (c) R_{xy} across all devices from the OOP field sweep measurement. (d) The normalised R_{xy}^{IP} in the $+H_x \rightarrow 0$ Oe quadrant is converted to $\cos^{-1} R_{xy}^{IP}$ to determine the device anisotropy. (e) The effective anisotropy field is then determined from the effective anisotropy energy $K_{u,eff}$ shown in the integrated area shaded in grey.

Hall angle θ_{SH} which represents the ratio of spin current density J_s to charge current density J_c , Pt has been reported to have $\theta_{SH,Pt} \approx +0.07$ while Ta has a comparatively larger spin Hall angle with opposite polarity of up to $|\theta_{SH,Ta}| = 0.15$ [10–12]. Sandwiching an FM layer with dissimilar HM layers has been demonstrated to further increase the overall SOT efficiency [13, 14]. Current-induced SOT switching is

also not limited to a single FM layer, and the magnetic volume V can be increased by repeating the bilayers without sacrificing PMA [15]. As these structures begin to become more complex, so does the interaction between SOT and the FM/HM multilayer (ML).

In this work, we investigate the effects of seed t_{seed} and interlayer $t_{interlayer}$ Pt thicknesses in Ta/Pt (t_{seed})/[Co/Pt

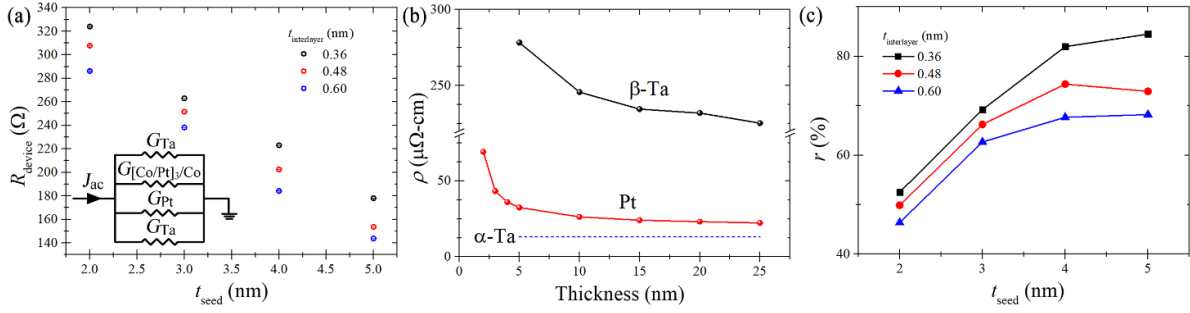


Figure 2. (a) Resistances of measured devices showing monotonic decrease in resistance as t_{seed} and $t_{\text{interlayer}}$ increases. Inset shows a circuit schematic of four-resistor approximation with respective conductance G_i , where i represents the Ta adhesion layer, Pt seed layer, [Co/Pt]₃/Co multilayer, and the Ta cap layer. (b) Resistivities ρ of Ta and Pt of varying thicknesses deposited on thermally oxidised Si substrate. α -Ta resistivity is shown for comparison [27]. (c) Ratio r of current through the Pt and Ta layers sandwiching the [Co/Pt]₃/Co multilayer.

($t_{\text{interlayer}}$)]₃/Co/Ta ml. The interlayer Pt modifies the interlayer exchange coupling (IEC) strength between Co layers, and can be used to tune the magnetic anisotropy. Using the harmonic lock-in technique, we measure the SOT efficiencies across varying t_{seed} and $t_{\text{interlayer}}$. We treat the [Co/Pt]₃/Co as a single FM unit layer and take into account the current density shunting through the thicker HM layers as well as the planar Hall effect (PHE) contribution to the SOT efficiency. We find that for this stack structure, the Pt layer that promotes PMA but also screens spin current originates from the bottom Ta layer. Consequently, tuning t_{seed} and $t_{\text{interlayer}}$ is a matter of compromise between PMA and SOT efficiency.

2. Experiment

Multilayer stacks of Ta (5)/Pt (t_{seed})/[Co (0.6)/Pt ($t_{\text{interlayer}}$)]₃/Co (0.6)/Ta (5) (nominal layer thicknesses in nanometers) were deposited at room temperature onto thermally oxidized Si wafers with oxide thickness of 300 nm using magnetron sputtering at a base pressure of better than 1.0×10^{-8} Torr. The numerical subscript represents the number of [Co/Pt] bilayer repeats. t_{seed} is the Pt seed thickness from 2 nm to 5 nm in 1 nm intervals, while $t_{\text{interlayer}}$ is the Pt interlayer thickness from 0.36 nm to 0.60 nm in 0.12 nm intervals. After deposition, the blanket films were patterned into Hall crosses comprising wires of 5 μm width and 20 μm length using electron beam lithography. Contact pads of Ta (5)/Cu (100)/Ta (5) were deposited for transport measurements.

To characterize the device, the transverse anomalous Hall resistance R_{xy} was measured across a sweeping in-plane (IP) H_x and out-of-plane (OOP) H_z external magnetic field, using a dc probing current $I_{\text{dc}} = 200 \mu\text{A}$ along the x axis while measuring the anomalous Hall voltage V_{xy} formed across the y axis. The V_{xy} and R_{xy} are related by $R_{xy} = V_{xy}/I_{\text{dc}}$. The R_{xy}^{OOP} (black) and R_{xy}^{IP} (red) hysteresis curves for all devices are available in the supplementary materials S1 (available online at <https://stacks.iop.org/JPhysD/53/505002/mmedia>). As R_{xy} is proportional to the out-of-plane magnetization component $M_z = \vec{M} \cos \theta$, where \vec{M} is the magnetization vector and θ is the magnetization polar angle, all samples showed square hysteresis in a sweeping H_z indicating PMA [16]. However,

in a sweeping H_x , certain devices show the in-plane to out-of-plane remanence $R_{xy}^{\text{IP}}/R_{xy}^{\text{OOP}}$ at $H_x = 0$ Oe to be below unity. For comparison, the IP hysteresis curves for ($t_{\text{interlayer}} = 0.36$ nm, $t_{\text{seed}} = 2$ nm) and ($t_{\text{interlayer}} = 0.36$ nm, $t_{\text{seed}} = 3$ nm) are plotted in figures 1(a) and (b), respectively.

The MagVision Kerr microscopy system was used in differential imaging mode to obtain the polar Kerr images. For devices with remanence below unity, dark (bright) domains in an oppositely contrasted magnetic background exist at $H_x = 0$ Oe, indicating a mix of upwards (downwards) magnetized domains. For devices with remanence close to unity, Kerr microscopy images show a more homogenous dark or bright contrast across the magnetic material of the devices. Generally, remanence approaches unity with thicker Pt seed layers, which can be attributed to reduced roughness, an improvement to the (111) texture, and subsequent reduction in Co/Pt interfacial roughness (see supplementary materials S2) [17, 18]. figure 1(c) shows R_{xy}^{OOP} for all devices. As the Pt seed layer thickness t_{seed} increases, its resistance decreases, and more current can shunt through it. This results in less current flowing through the [Co/Pt] multilayer [19]. Furthermore, R_{xy} across devices with $t_{\text{interlayer}} = 0.36$ nm and 0.60 nm are almost identical, while devices with $t_{\text{interlayer}} = 0.48$ nm have a smaller R_{xy}^{OOP} . Several factors that affect the multilayer interface as well as interactions between the ultrathin Co and Pt layers are discussed in supplementary materials S3.

Devices with $t_{\text{interlayer}} = 0.48$ nm show that $H_{k,\text{eff}}$ scales with t_{seed} , while that of $t_{\text{interlayer}} = 0.36$ nm and 0.60 nm show peak $H_{k,\text{eff}}$ at $t_{\text{seed}} = 4$ nm. The $H_{k,\text{eff}}$ for each multilayer stack was determined using the normalised R_{xy}^{IP} from the $+H_x \rightarrow 0$ Oe quadrant as shown in the exemplary curve in figure 1(d). The inset shows the conversion to normalised $\cos^{-1} R_{xy}^{\text{IP}}$ and the shaded region represents the effective anisotropy $K_{u,\text{eff}}$. $H_{k,\text{eff}}$ was then determined for all of the devices and summarized in figure 1(e). The $H_{k,\text{eff}}$ peaks at $t_{\text{seed}} = 4$ nm with the exception of devices with $t_{\text{interlayer}} = 0.48$ nm, which exhibited monotonic increase with t_{seed} . In general, a thicker Pt seed layer t_{seed} would yield [Co/Pt] multilayers with stronger PMA [20]. However, the effective anisotropy field $H_{k,\text{eff}}$ peaks at $t_{\text{seed}} = 4$ nm and noticeably decreases for $t_{\text{seed}} = 5$ nm as a result of increased surface and interface roughness

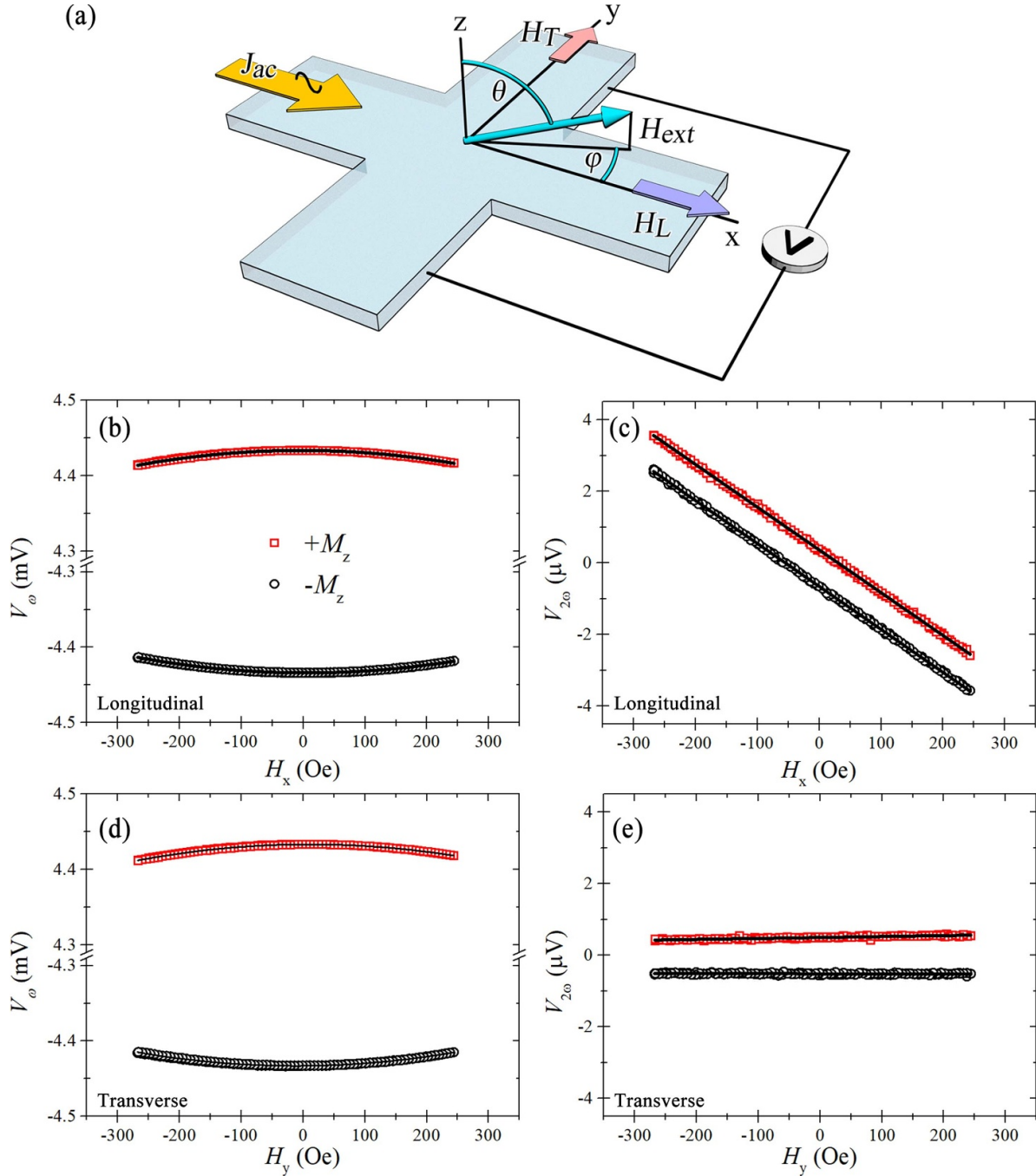


Figure 3. (a) Schematic set up for harmonic lock-in measurement of a Hall cross structure with coordinate system, where θ and φ are the polar and azimuthal angles, respectively. (b), (d) First harmonics V_{ω} measurements in the longitudinal and transverse schemes, respectively. (c), (e) Second harmonics $V_{2\omega}$ measurement in the longitudinal and transverse schemes, respectively.

with increasing t_{seed} [21]. The roughness is exacerbated for subsequently deposited layers of Co and Pt, and can lead to undesirable ‘orange-peel’ coupling, leading to the decrease in $H_{k,eff}$ observed for devices with $t_{interlayer} = 0.36$ and 0.60 nm [22].

When performing electrical measurements, the various thin film layers will conduct fractional current densities J due to their individual electrical resistivities and thicknesses. Assuming four resistors in parallel for each layer $i = \text{Ta}$ (adhesion), Pt, FM, Ta (cap), we approximate the current

shunting through each layer by noting that the conductance of the entire device G_{device} is the sum of all individual layer conductances G_i ,

$$G_{device} = \sum G_i = \sum \frac{t_i w}{\rho_i l} \quad (1)$$

where t_i is the thickness, and ρ_i is the resistivity of layer i . Here, we treat the $[\text{Co/Pt}]_3/\text{Co}$ multilayer as one perpendicularly magnetized FM layer and assume that the voltage across each layer i is the same. The individual device resistances

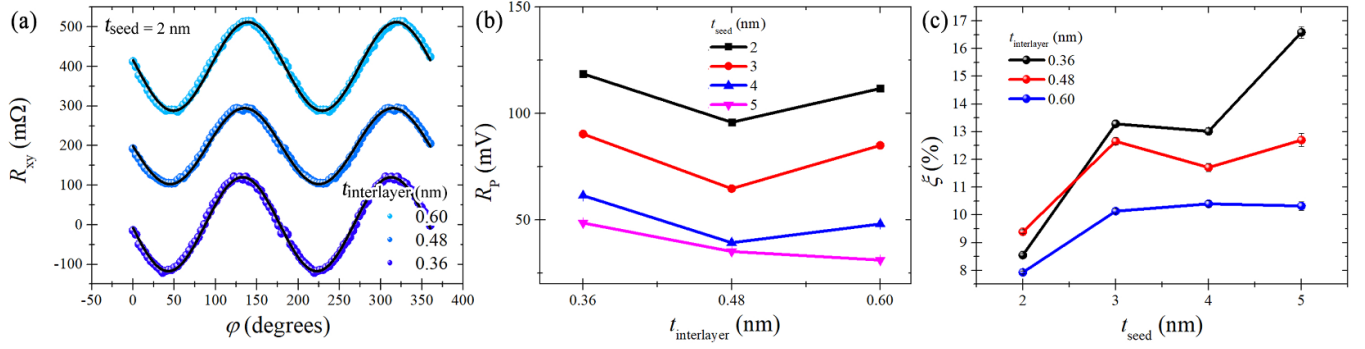


Figure 4. (a) φ -dependent ($\theta \approx 90^\circ$) R_{xy} curves fitted with equation (1) for $t_{seed} = 2$ nm. (b) R_p and (d) $\xi = R_p/R_A$ across all devices with t_{seed} and $t_{interlayer}$.

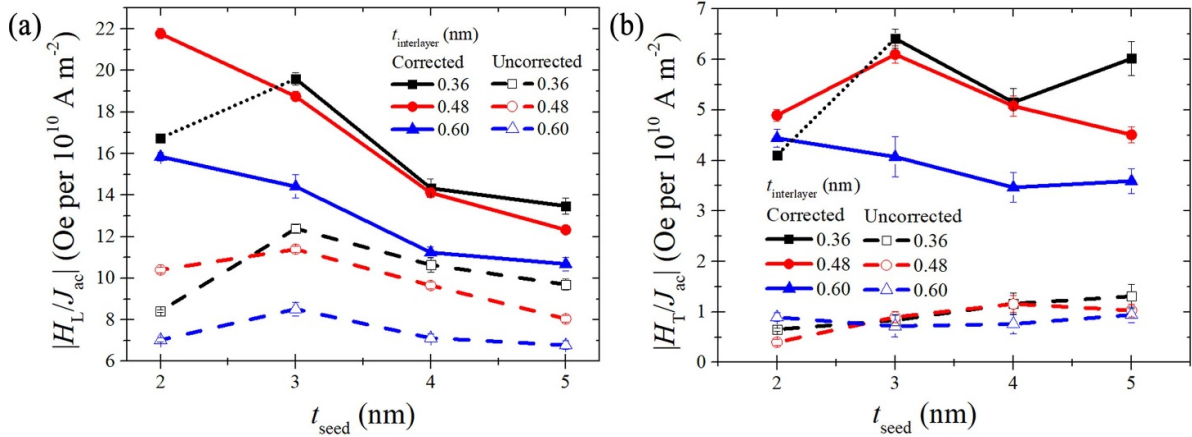


Figure 5. Uncorrected SOT efficiencies (dashed lines) accompanied by current-density and PHE-corrected SOT efficiencies for (a) longitudinal and (b) transverse efficiencies. The corrections result in efficiencies several times larger than uncorrected values.

were measured and plotted in figure 2(a). The inset illustrates the circuit for each device with each layer having its own conductance values G_i . From this information, we can account for the current density through the HMs. The current density through layer i can be determined from the ratio of conductance $r_i = G_i/\Sigma G_i$, so that the current density through each layer scales as $J_i = r_i J$.

Subsequently, in order to determine the resistivities of the HM layers, we deposited varying thicknesses of Ta and Pt onto a thermally oxidised Si substrate. The sheet resistances for Ta and Pt were measured using the in-line four-point probe method and plotted in figure 2(b). The resistivities ρ scale approximately as a reciprocal to film thickness t , with values close to those reported elsewhere [23–25]. The sputtered Ta films are noticeably resistive, indicating that they form the tetragonal β -Ta phase that has strong spin-orbit coupling [23, 26]. In comparison, the blue dashed line indicates the resistivity of α -Ta of about $13 \mu\Omega\text{-cm}$ [23, 27]. We use the measured β -Ta resistivity for the adhesion and capping Ta layers [10, 28]. As t_{seed} increases in thickness, more current is permitted to flow through the HM layer. The ratio r of current flowing through the HM layers that contribute to the SOT is determined and plotted in figure 2(c). More current is shunted through the HM layers with a thicker t_{seed} or a thinner $t_{interlayer}$.

Next, we quantify the SOT damping-like (longitudinal) H_L and field-like (transverse) H_T effective fields for varying t_{seed} and $t_{interlayer}$ using the harmonic lock-in technique [29, 30]. A Keithley 6221 was used to source an ac current density with amplitude ranging from 8×10^8 to 8×10^9 A m $^{-2}$ in intervals of 1×10^8 A m $^{-2}$. A Signal Recovery 7265 lock-in amplifier was used to detect the first and second harmonic Hall voltages simultaneously. A small bias field of 400 Oe in the z direction was present to prevent the formation of domains. The measurement set-up is illustrated in figure 3(a). When an in-plane current is injected along the x axis, a transverse spin current from the HM layers diffuse into the FM multilayer. Due to the opposite spin Hall angles of Pt and Ta and the structural inversion asymmetry, a net spin torque acts on the FM. Using a sinusoidal current to adiabatically oscillate the magnetization, we measure the first V_ω and second $V_{2\omega}$ harmonic Hall voltages across a range of current densities J_{ac} as a function of external longitudinal and transverse fields H_x and H_y , respectively.

Exemplary curves of the longitudinal and transverse V_ω and $V_{2\omega}$ are shown in figures 3(b)–(e). Both longitudinal and transverse V_ω measurements show similar parabolic characteristics. However, the longitudinal and transverse $V_{2\omega}$ have different linear behaviours, as shown in figures 3(d) and (f). The substantially larger longitudinal $V_{2\omega}$ is indicative of a

dominant SHE, while the significantly smaller slope of the transverse $V_{2\omega}$ is indicative of the negligible Rashba contribution [31]. The longitudinal $V_{2\omega}$ has negative slopes for up and down magnetized states $\pm M_z$. In contrast, the transverse $V_{2\omega}$ has different slopes and relatively smaller magnitude for up and down magnetized states $\pm M_z$. V_{ω} and $V_{2\omega}$ are fitted using quadratic and linear fitting functions, respectively. The following relation is then used to determine H_L and H_T :

$$H_{L(T)} = -2 \frac{\partial V_{2\omega}}{\partial H_{x(y)}} / \frac{\partial^2 V_{\omega}}{\partial H_{x(y)}^2}. \quad (2)$$

In order to account for the in-plane magnetic field Hall resistance, i.e. PHE, φ -dependent ($\theta \approx 90^\circ$) measurements were performed using an in-plane field $H_{IP} = 4$ kOe. The Hall resistance can be expressed as:

$$R_{xy} = R_A \cos \theta + R_P \sin^2 \theta \sin 2\varphi \quad (3)$$

where R_A and R_P are the anomalous and planar Hall resistances, respectively. The individual curves are then fitted to obtain R_P and the PHE/AHE ratio $\xi = R_P/R_A$, which is then used to determine the modified, PHE-corrected SOT efficiencies $H'_{L(T)}$ given by [32]:

$$H'_{L(T)} = \frac{H_{L(T)} \pm 2\xi H_{T(L)}}{1 - 4\xi^2}.$$

Due to imperfect alignment between the sample plane and the field, a small out-of-plane field component is present as the sample rotates about the z axis. This is resolved by averaging the planar Hall resistance at θ and $\theta + \pi$ as shown in the φ -dependent R_{xy} curves plotted and fitted using equation (1) in figure 4(a) for devices with $t_{seed} = 2$ nm.

The PHE- and current-corrected $H'_{L(T)}/J_{ac}$ are shown in figure 5. We find that after accounting for both corrections, H'_L/J_{ac} and H'_T/J_{ac} are several times larger as compared to their uncorrected values. The magnitude of H'_L/J_{ac} is greater than that of H'_T/J_{ac} , indicating that the SOT is predominantly due to the SHE mechanism [33, 34]. At its thinnest range of $t_{seed} = 2$ nm, the film stacks demonstrate R_{xy}^{IP}/R_{xy}^{OOP} below unity at $H_x = 0$ Oe. In particular, the measured SOT efficiency for the device with $t_{seed} = 2$ nm and $t_{interlayer} = 0.36$ nm shows an anomalous SOT efficiency. This is attributed to ineffective (111) texturing of Co by the thin Pt seed layers, as thicker t_{seed} and $t_{interlayer}$ generally improved the in-plane and out-of-plane remanence ratio $R_{xy}^{IP}/R_{xy}^{OOP} \approx 1$ so that the magnetization completely returns to one of the bistable (up or down) states at $H_x = 0$ Oe [35]. From our measurements, we observe that the damping- and field-like efficiencies are inversely related to t_{seed} and $t_{interlayer}$. The high-resistivity β -Ta layer generates substantial SOT [36, 37]. Due to the opposite spin Hall angle with respect to the adjacent Pt seed layer [38], the spin current from the β -Ta layer gets screened. Consequently, the net spin current from the

opposite contributions of the β -Ta/Pt HM bilayer decreases with increasing Pt seed layer thickness t_{seed} . Similarly, thicker $t_{interlayer}$ leads to greater spin scattering across the multilayers [39–41]. From the damping-like field efficiency $|H_L/J_{ac}|$ plot, the seed and interlayer Pt layers can be observed to screen the spin current from the bottom Ta layer as t_{seed} and $t_{interlayer}$ increase in thickness. However, there is no appreciable correlation between the already small transverse field efficiency $|H_T/J_{ac}|$.

3. Conclusions

In this work, we have studied perpendicularly magnetized multilayers of Ta/Pt/[Co/Pt]₃/Co/Ta with varying Pt seed and interlayer thicknesses. The Pt interlayer thickness influences the IEC between the Co layers. Consequently, this affects the Pt seed thickness dependence on the anisotropy. It was determined from R_{xy} - H_x measurements that $t_{seed} \geq 3$ nm was necessary to achieve remanence close to unity. *In-situ* Kerr microscopy images confirm this observation. The SOT efficiencies for all devices were then measured with current density and PHE-correction taken into account. The damping-like efficiency scales inversely with Pt seed and interlayer thicknesses, indicating that the spin current from the bottom Ta layer gets screened from both. As such, there is a compromise between PMA and SOT efficiency, as the SOT efficiencies decrease with increasing t_{seed} and $t_{interlayer}$ thicknesses.

Acknowledgments

The work was supported by the Singapore National Research Foundation, under a Competitive Research Programme (Non-volatile Magnetic Logic and Memory Integrated Circuit Devices, NRF-CRP9-2011-01), and an Industry-IHL Partnership Program (NRF2015- IIP001-001). The support from an RIE2020 ASTAR AME IAF-ICP Grant (No. I1801E0030) is also acknowledged.

ORCID iDs

Gerard Joseph Lim

 <https://orcid.org/0000-0003-2411-5841>

Weiliang Gan

 <https://orcid.org/0000-0001-9278-0718>

References

- [1] Miron I M, Garello K, Gaudin G, Zermatten P-J, Costache M V, Auffret S, Bandiera S, Rodmacq B, Schuhl A and Gambardella P 2011 *Nature* **476** 189
- [2] Lim S T, Tran M, Chenchen J W, Ying J F and Han G 2015 *J. Appl. Phys.* **117** 17A731
- [3] Peng S et al 2017 *Appl. Phys. Lett.* **110** 072403
- [4] Johnson M T, Bloemen P J H, Den Broeder F J A and De Vries J J 1996 *Rep. Prog. Phys.* **59** 1409
- [5] Lin C J, Gorman G L, Lee C H, Farrow R F C, Marinero E E, Do H V, Notarys H and Chien C J 1991 *J. Magn. Magn. Mater.* **93** 194

- [6] Chowdhury P, Kulkarni P D, Krishnan M, Barshilia H C, Sagdeo A, Rai S K, Lodha G S and Rao D V S 2012 *J. Appl. Phys.* **112** 023912
- [7] Lee O J, Liu L Q, Pai C F, Li Y, Tseng H W, Gowtham P G, Park J P, Ralph D C and Buhrman R A 2014 *Phys. Rev. B* **89** 024418
- [8] Baek S-H C, Park K-W, Kil D-S, Jang Y, Park J, Lee K-J and Park B-G 2018 *Nat. Electron.* **1** 398
- [9] Lim G J, Chua D, Gan W, Murapaka C and Lew W S 2020 *Adv. Electron. Mater.* **6** 1901090
- [10] Liu L, Pai C-F, Li Y, Tseng H W, Ralph D C and Buhrman R A 2012 *Science* **336** 555
- [11] Liu L, Buhrman R A and Ralph D C 2011 Review and analysis of measurements of the spin Hall effect in platinum arXiv:1111.3702
- [12] Liu L, Lee O J, Gudmundsen T J, Ralph D C and Buhrman R A 2012 *Phys. Rev. Lett.* **109** 096602
- [13] Wong Q Y, Murapaka C, Law W C, Gan W L, Lim G J and Lew W S 2019 *Phys. Rev. Appl.* **11** 024057
- [14] Wang R, Xiao Z, Liu H, Quan Z, Zhang X, Wang M, Wu M and Xu X 2019 *Appl. Phys. Lett.* **114** 042404
- [15] Huang K-F, Wang D-S, Lin -H-H and Lai C-H 2015 *Appl. Phys. Lett.* **107** 232407
- [16] Nagaosa N, Sinova J, Onoda S, MacDonald A H and Ong N P 2010 *Revs. Mod. Phys.* **82** 1539
- [17] Mathet V, Devolder T, Chappert C, Ferré J, Lemerle S, Belliard L and Guentherodt G 2003 *J. Magn. Magn. Mater.* **260** 295
- [18] Takemura Y, Lee D-Y, Lee S-E and Park J-G 2016 *Nanotechnology* **27** 485203
- [19] Ghosh A, Garello K, Avci C O, Gabureac M and Gambardella P 2017 *Phys. Rev. Appl.* **7** 014004
- [20] Huang J C A, Chen M M, Lee C H, Wu T H, Wu J C and Fu C M 2002 *J. Magn. Magn. Mater.* **239** 326
- [21] Lim J-E, Jeong J K, Ahn K H, Kim H J, Hwang C S, Park D-Y and Lee D-S 2004 *J. Mater. Res.* **19** 460
- [22] Moritz J, Garcia F, Toussaint J C, Dieny B and Nozières J P 2004 *Europhys. Lett. (EPL)* **65** 123
- [23] Rossnagel S M 2002 *J. Vac. Sci. Technol. B* **20** 2328
- [24] Zhang J, Huai Y, Chen L and Zhang J 2003 *J. Vac. Sci. Technol. B* **21** 237
- [25] Agustsson J S, Arnalds U B, Ingason A S, Gylfason K B, Johnsen K, Olafsson S and Gudmundsson J T 2008 *J. Phys. Conf. Ser.* **100** 082006
- [26] Wong Q Y, Gan W L, Luo F L, Lim G J, Ang C C I, Tan F N, Law W C and Lew W S 2018 *J. Phys. D: Appl. Phys.* **51** 115004
- [27] Baker P N 1972 *Thin Solid Films* **14** 3
- [28] Woo S, Mann M, Tan A J, Caretta L and Beach G S D 2014 *Appl. Phys. Lett.* **105** 212404
- [29] Pi U H, Won Kim K, Bae J Y, Lee S C, Cho Y J, Kim K S and Seo S 2010 *Appl. Phys. Lett.* **97** 162507
- [30] Garello K, Miron I M, Avci C O, Freimuth F, Mokrousov Y, Blügel S, Auffret S, Bouille O, Gaudin G and Gambardella P 2013 *Nat. Nanotechnol.* **8** 587
- [31] Yang M et al 2016 *Sci. Rep.* **6** 20778
- [32] Hayashi M, Kim J, Yamanouchi M and Ohno H 2014 *Phys. Rev. B* **89** 144425
- [33] Martinez E, Emori S and Beach G S D 2013 *Appl. Phys. Lett.* **103** 072406
- [34] Amin V P and Stiles M D 2016 *Phys. Rev. B* **94** 104420
- [35] Wang K, Wu M-C, Lepadatu S, Claydon J S, Marrows C H and Bending S J 2011 *J. Appl. Phys.* **110** 083913
- [36] Hao Q and Xiao G 2015 *Phys. Rev. B* **91** 224413
- [37] Cecot M, Karwacki Ł, Skowroński W, Kanak J, Wrona J, Żywczak A, Yao L, van Dijken S, Barnaś J and Stobiecki T 2017 *Sci. Rep.* **7** 968
- [38] Phu P, Yamanoi K, Ohnishi K, Hyodo J, Rogdakis K, Yamazaki Y, Kimura T and Kurebayashi H 2019 *J. Magn. Magn. Mater.* **485** 304
- [39] Rojas-Sánchez J C, Reyren N, Laczkowski P, Savero W, Attané J P, Deranlot C, Jamet M, George J M, Vila L and Jaffrès H 2014 *Phys. Rev. Lett.* **112** 106602
- [40] Nguyen M-H, Pai C-F, Nguyen K X, Muller D A, Ralph D C and Buhrman R A 2015 *Appl. Phys. Lett.* **106** 222402
- [41] Zhang W, Han W, Jiang X, Yang S-H and Parkin S S P 2015 *Nat. Phys.* **11** 496